Statistics of Intrinsic FMRI Data

Daniel B. Rowe[1]
[1]Marquette University, 1250 W. Wisconsin Avenue, Milwaukee, WI 53233

Abstract

In fMRI, it is often assumed that fMRI data are normally distributed in real and imaginary parts which lead to Ricean distributed in magnitude, which is approximately normal when the signal-to-noise ratio is large. Here, two fMRI data sets were acquired to examine this assumption. Both data sets image a plastic sphere containing an agarose gel. The first data set utilizes a typical fMRI pulse sequence to acquire data except the RF which produces the signal is omitted. The resulting data should be purely normally distributed noise in real and imaginary parts. Subsequently, a second data set is acquired with the same pulse sequence except the RF was not omitted. The resulting data should be normally distributed in real and imaginary parts which lead to Ricean distributed in magnitude. The noise properties of the data are explored.

Key Words: MRI, fMRI, voxel distribution, activation

1. FMRI Data Acquisition

1.1 FMRI Background

Magnetic resonance imaging (MRI) is a non-invasive technique for peering inside the human body. MRI has been remarkable at providing physicians and scientists with anatomical images that can be used to treat ailments and improve the health of their patient. MRI uses a specifically designed machine depicted in Figure 1 (left) that uses very strong static electromagnets and weaker magnetic field gradients to sample the spatial frequencies, called *k*-space, for slice images that form a volume image as depicted in Figure 1 (right).

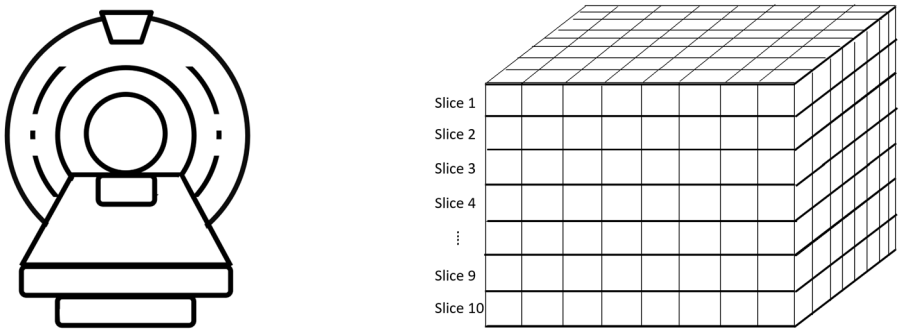

Figure 1: MRI machine (left) and volume of slices (right).

Functional magnetic resonance imaging (fMRI) is a variant with much higher temporal resolution but much lower spatial resolution. In fMRI, the weaker magnetic field gradients called a pulse sequence depicted in Figure 2 (left) are applied which result in the switching of the *k*-space trajectory "left-right" to "travel" along different rows of *k*-space with in-between phase encodes to "increment" rows as in Figure 2 (right). In fMRI, we must travel along a trajectory like the Pac-Man game. There is no jumping to other locations. Along each row, while gradients are switching, analog-to-digital converters (ADCs) measure the current in a "wire" with independent normally distributed thermal noise. The measurement of the current in the wire translates to a spatial frequency amplitude coefficient measurement for an image. The array of spatial frequency amplitude coefficient measurements is discrete inverse Fourier transformed, which is a linear

orthogonal process. The ADCs take current measurements with independent and identically normally distributed errors, the spatial frequency amplitude coefficients are normally distributed, and since the inverse Fourier transform is orthogonal, the voxel measurements should also be independent and identically normally distributed.

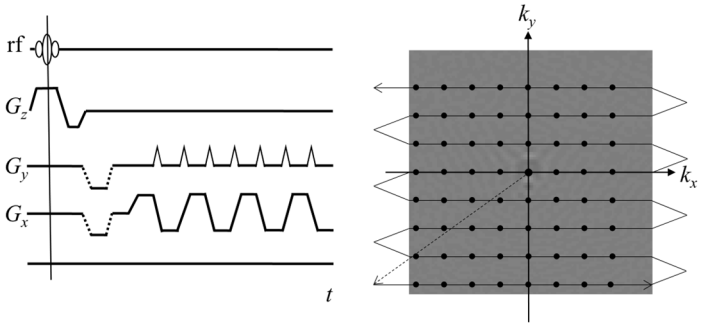

Figure 2: MRI machine (left) and volume of slices (right).

1.2 FMRI Data Sets

To examine the statistical distribution of fMRI data, two data sets are acquired. For this data, a 3.0 T General Electric Signa LX magnetic resonance imager was used to image a plastic phantom sphere filled with an agarose gel as depicted in Figure 3 (left). Common parameters for both scans were echo time TE=84.1 ms, field of view FOV=192 mm, effective echo spacing $EESP$=0.864 ms, using a single channel coil n_c=1, for n_z=10 slices. Each image had a matrix size of n_x=96 and n_y=96, for n_t=138 time points. In data set one labeled RF Off the radio frequency pulse in the top of Figure 2 (left) is set to RF=0º while in data set two labeled RF On is set to RF=90º. The RF tilts the magnetization depicted by the blue arow in Figure 3 (right) into the transverse x-y plane. The intensity level measured in each voxel in functional MRI is an aggregate measure of the transverse relaxation projection of the magnetic moment (blue vector) in Figure 3 (right) into the horizontal x-y plane (Huttel et al., 2004), denoted as T_2*. Anatomical images typically use the longitudinal projection of the magnetic moment (blue vector) in Figure 3 (right) into the z axis, denoted as T_1.

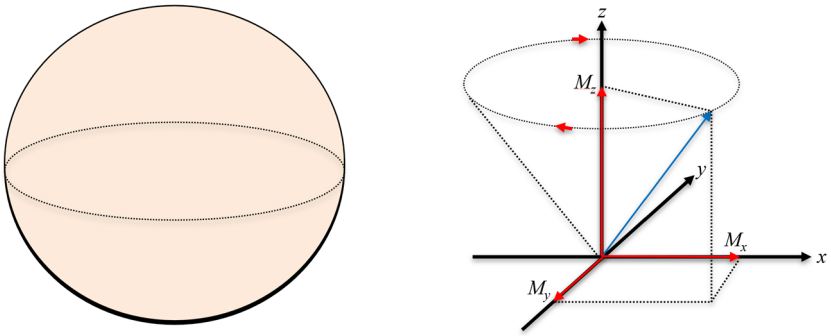

Figure 3: Phantom sphere filled with agarose gel (left) magnetic relaxations (right).

It is well-known that when an array of k-space measurements as depicted in Figure 2 (right) are inverse discrete Fourier transformed, that the reconstructed images are complex-valued (real and imaginary) due to the lack of Hermitian symmetry and because the relationship between image space and k-space is not exactly a Fourier transform (Rowe, 2016) as written in Equation 1.

$$s(k_x, k_y \mid t) = \int_{-\infty}^{+\infty}\int_{-\infty}^{+\infty} \rho(x,y) e^{-t/T_2^*(x,y)} e^{-i\gamma\Delta B(x,y)t} e^{-i2\pi(k_x x + k_y y)} dxdy \quad [1]$$

When the RF is off, no signal is produced or measured and the voxel measurements in the volume image are pure independent and identically distributed normal noise with a mean of zero (no signal). When the RF is on, the signal is produced and the voxel measurements in the volume image should be independent and identically distributed noise with constant mean within the phantom (mean of μ) and zero mean outside. In each voxel, the real and imaginary parts are $y_R \sim N(\mu_R,\sigma^2)$ and $y_I \sim N(\mu_I,\sigma^2)$ as in Equation 2 where $\mu_R=\rho\cos\theta$ and $\mu_I=\rho\sin\theta$.

$$f(y_R, y_I) = \frac{1}{(2\pi\sigma^2)^{1/2}} \exp\left[-\frac{(y_R-\mu_R)^2}{2\sigma^2}\right] \frac{1}{(2\pi\sigma^2)^{1/2}} \exp\left[-\frac{(y_I-\mu_I)^2}{2\sigma^2}\right] \quad [2]$$

In fMRI we are interested in the magnitude of the complex-valued voxel values, so a transformation from random variables (y_R, y_I) to (r,ϕ) where $y_R=r\cos(\phi)$, $y_I=r\sin(\phi)$, with Jacobian is $J=r$ is performed to arrive at a joint distribution

$$f(r,\phi) = \frac{r}{2\pi\sigma^2} \exp\left\{-\frac{1}{2\sigma^2}\left[r^2+\rho^2-2r\rho\cos(\phi-\theta)\right]\right\}. \quad [3]$$

From this, the Ricean marginal distributions

$$f(r) = \frac{r}{\sigma^2} \exp\left\{-\frac{r^2+\rho^2}{2\sigma^2}\right\} I_0\left(\frac{r\rho}{\sigma^2}\right) \quad [4]$$

for the magnitude and unnamed non-normal distribution

$$f(\phi) = \frac{1}{2\pi} \exp\left[-\frac{\rho^2}{2\sigma^2}\right]\left[1+\frac{\rho}{\sigma}\sqrt{2\pi}\cos(\phi-\theta)\exp\left[\frac{\rho^2\cos^2(\phi-\theta)}{2\sigma^2}\right]\Phi\left(\frac{\rho\cos(\phi-\theta)}{\sigma}\right)\right] \quad [5]$$

for the phase can be found. When the signal ρ is zero (i.e. in empty space voxels of an fMRI) , the Ricean distribution becomes the Rayleigh distribution and when signal ρ is very large (in high intensity voxels in the brain), it becomes the normal distribution. When the signal ρ is zero (i.e. in empty space voxels of an fMRI), the unnamed non-normal distribution becomes the uniform distribution between $-\pi$ and π and when signal ρ is very large (in high intensity voxels in the brain) it becomes the normal distribution.

The magnitude images of the n_z=10 slices through the spherical agar phantom with the RF=90º on are displayed in Figure 4 with fiducial reference "circles." The reference circles were made by averaging the n_t=138 volume images of the time series and setting those voxels above 0.25 of the maximum intensity to be inside and those below to be outside. Later, the voxels within and outside these circles will be analyzed for distributional properties.

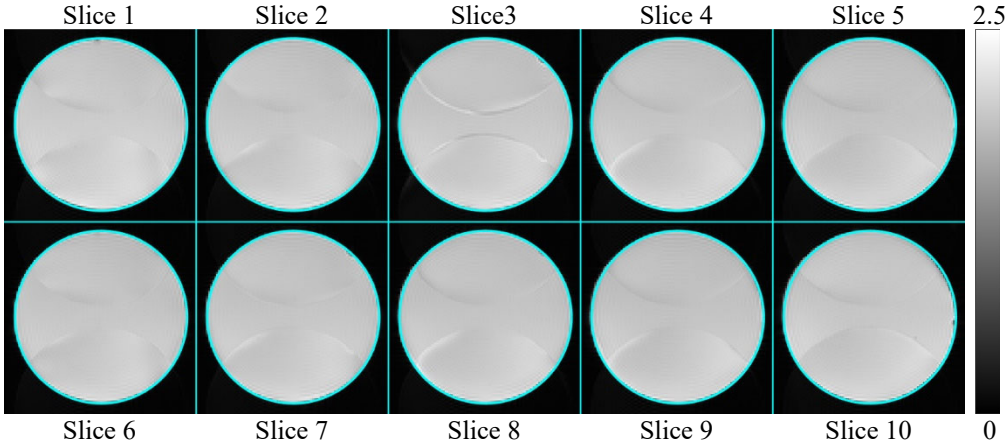

Figure 4: Average magnitudes of the ten slice images of the spherical agar phantom.

2. FMRI RF Off No Signal Data

After inverse Fourier transform reconstruction of the RF off *k*-space data, the images are complex valued. The distribution of the magnitude and phase of the RF off fMRI data set will be examined in this section. The distribution of the voxel's magnitude, phase, correlation between their real and imaginary channels, and autocorrelation will be discussed.

2.1 Magnitude and Phase

The magnitude of the complex-valued slice images for the first time point, t=1, is presented in Figure 5. The magnitude images for all subsequent time points appear visually similar. Note that the magnitude values in the voxels both inside the phantom and outside are near zero. This illustrates the fact that the RF is off and that pure noise is being measured. If the real and imaginary parts of the images are pure independent and identically distributed normal noise, then the distribution of the magnitude should be Rayleigh.

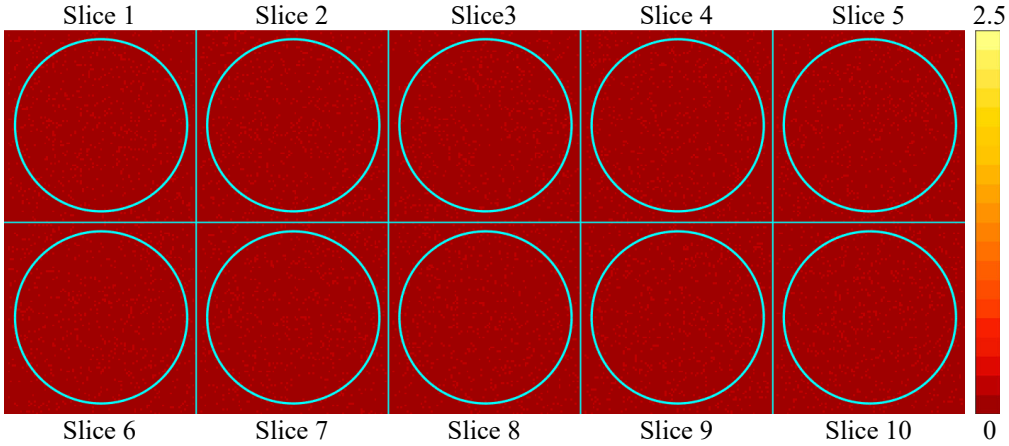

Figure 5: Magnitude slices of spherical agar phantom with RF off.

The phase of the complex-valued images for the first time point, t=1, is presented in Figure 6. The phase images for all subsequent time points appear visually similar. Note that the phase values in the voxels both inside the phantom and outside appear random between $-\pi$ and π. This illustrates the fact that the RF is off and that pure noise is being measured. If the real and imaginary parts of the images are pure independent and identically distributed normal noise, then the distribution of the phase should be uniform between $-\pi$ and π.

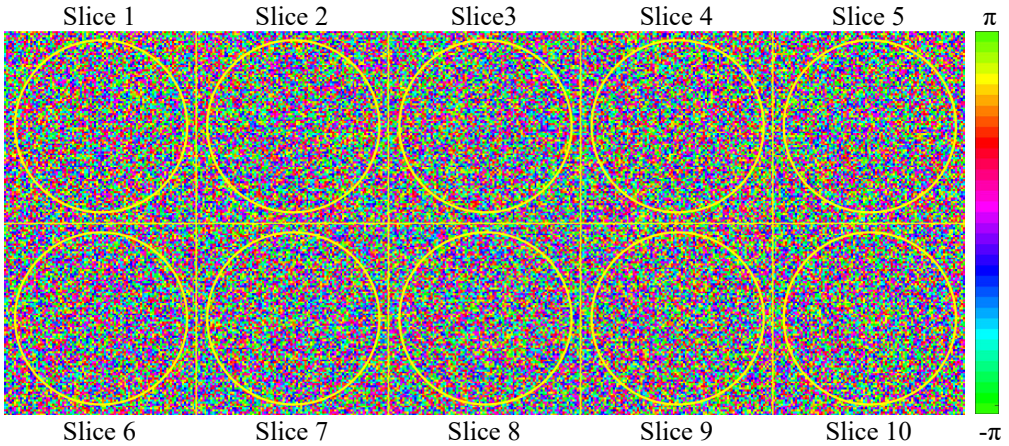

Figure 6: Phase slices of spherical agar phantom with RF off.

For the n_z=10 slices of the n_t=138 volume images, voxels were partitioned to be either inside the phantom or outside. Histograms of the voxels magnitudes both the within and outside the phantom from all slices are in Figure 7 (left) along with the superimpose of the theoretical Rayleigh distribution. Note that the histograms of within and outside are nearly identical and overlapping with the superimposed theoretical Rayleigh distribution fitting very well. This indicates that the real and imaginary parts of the images are pure independent and identically distributed normal noise.

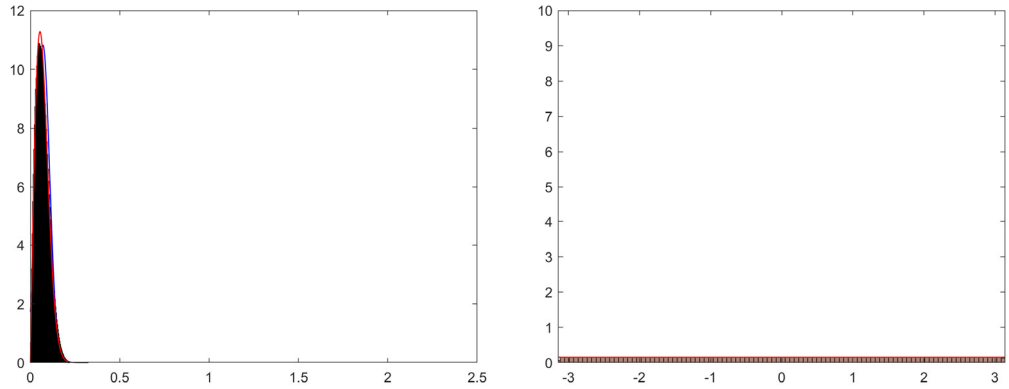

Figure 7: RF off histograms of magnitude (left) and phase (right) of spherical agar phantom.

Histograms of the voxels phases both the within and outside the phantom from all slices are in Figure 7 (right) along with the superimpose of the theoretical uniform distribution. Note that the histograms of within and outside the phantom are nearly identical and overlapping with the superimposed theoretical uniform between $-\pi$ and π distribution fitting very well. This indicates that the real and imaginary parts of the images are pure independent and identically distributed normal noise.

2.2 Real-Imaginary and AR(1) Correlations

In each voxel, there is a complex-valued time series formed from the series of complex-valued volume images. In each voxel of the n_z=10 slices, the correlation between the real and imaginary time series of length was computed and displayed in Figure 8. Note that in every voxel whether inside or outside the phantom the real-imaginary correlation is near zero. This indicates that the real and imaginary parts of the images are pure independent and identically distributed normal noise.

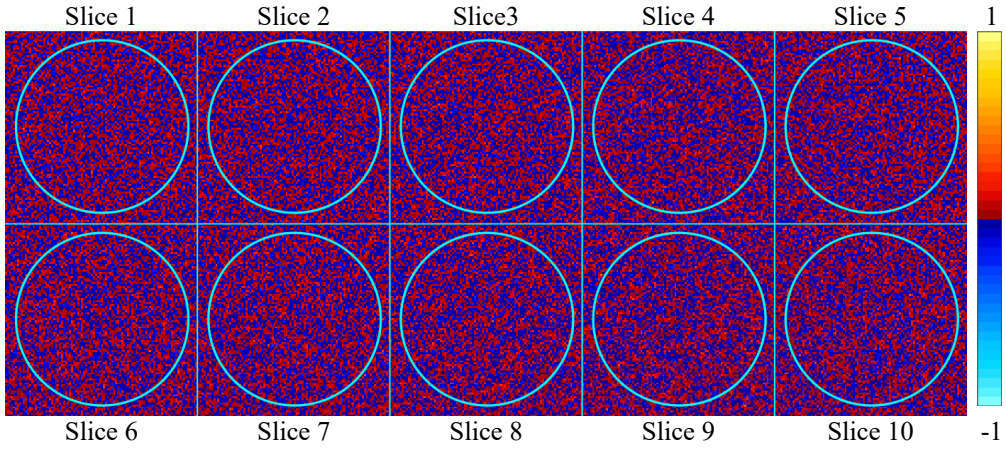

Figure 8: Real-imaginary correlation of spherical agar phantom with RF off.

In each voxel, the magnitude of the complex-valued time series was taken and the AR(1) autocorrelation computed as in Figure 9. Note that in every voxel whether inside or outside the phantom the magnitude AR(1) autocorrelation is near zero. This indicates that the real and imaginary parts of the images are pure independent and identically distributed normal noise.

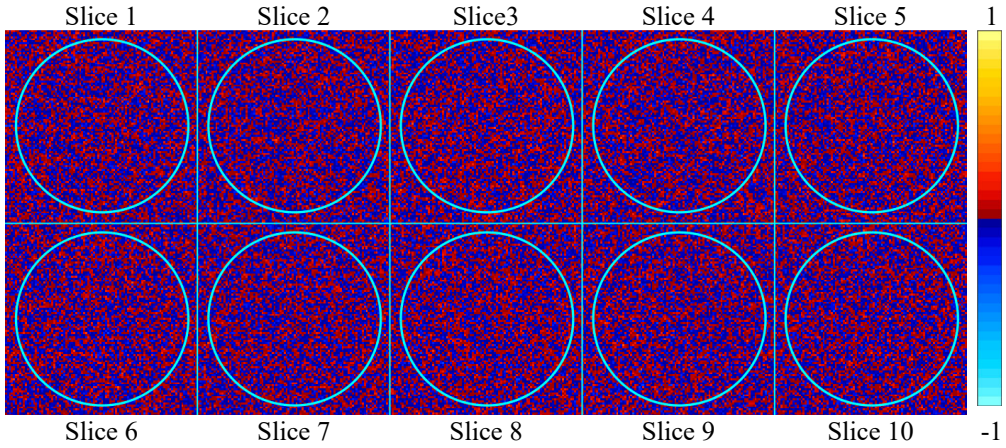

Figure 9: AR(1) magnitude correlation of spherical agar phantom with RF off.

To further examine these correlations, histograms were made. In Figure 10 (left) we can see that the real-imaginary correlations are centered about zero and appear to match the null hypothesis theoretical distribution superimposed in red. In Figure 10 (right) we can see that the AR(1) correlations in each voxel are centered about zero and appear to match the null hypothesis theoretical distribution superimposed in red. This indicates that the real and imaginary parts of the images are pure independent and identically distributed normal noise.

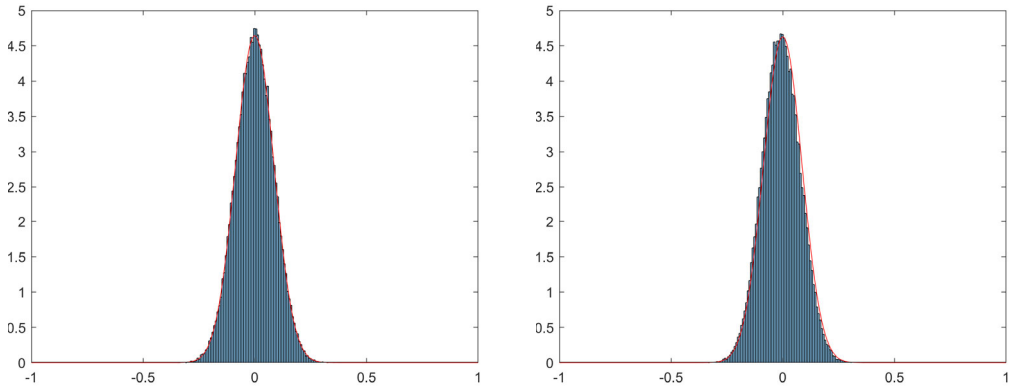

Figure 10: RF off histograms of real-imaginary (left) and AR(1) (right) correlations of the of spherical agar phantom.

From the graphical results presented in Figures 5-10, there is significant evidence to support the theoretical results that the complex-valued noise in voxels are independent and identically distributed from a normal distribution.

3. FMRI RF Off No Signal Data Plus Simulated Signal

Using the complex-valued images in Section 2 with RF off, constant magnitude signal equal to the average value observed within the phantom when the RF is on in Section 4 was added to each slice the average of which is 1.93. This is an intermediate step before examining data when the RF is on in Section 4. The distribution of the voxel's magnitude, phase, correlation between their real and imaginary channels, and autocorrelation will be discussed.

3.1 Magnitude and Phase

The magnitude of the complex-valued slice images for the first time point, t=1, is presented in Figure 11. The magnitude images for all subsequent time points appear visually similar. Note that the magnitude values in the voxels inside the phantom are around 1.93 and outside are near zero.

This illustrates the fact that the RF is simulated being on, and that signal plus noise is being measured inside while pure noise is being measured outside. If the real and imaginary parts of the images are independent and identically distributed normal noise with constant mean, then the distribution of the magnitude should be Ricean distributed inside and outside should be Rayleigh as in Section 2.

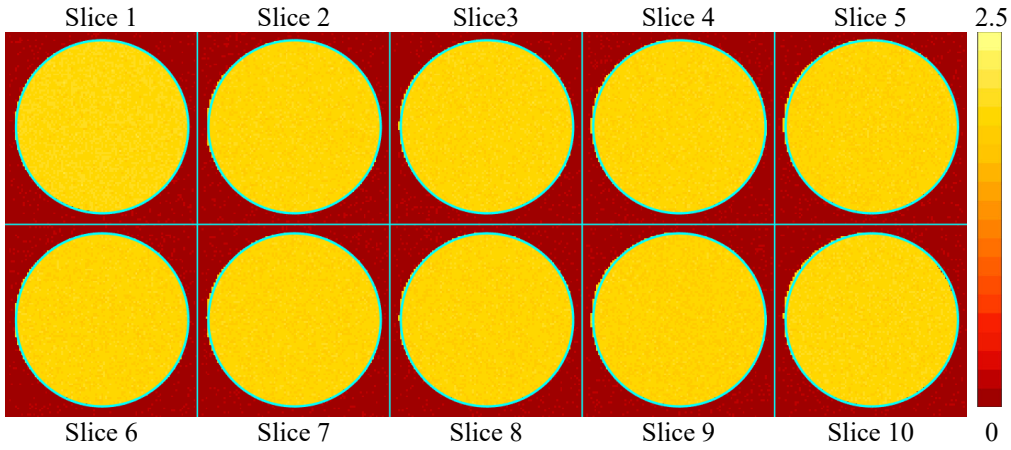

Figure 11: Magnitude slices of spherical agar phantom with RF off plus signal.

The phase of the complex-valued images for the first time point, t=1, is presented in Figure 12. The phase images for all subsequent time points appear visually similar. Note that the phase values in the voxels inside the phantom have a mean near zero and outside appear random between $-\pi$ and π as in Section 2. This illustrates the fact that the RF is simulated as on with no added phase inside the phantom and that pure noise is being measured outside. If the real and imaginary parts of the images are independent and identically distributed normal noise with a constant magnitude inside, then the distribution of the phase inside is not uniform but peaked about its mean (Rowe and Logan, 2004) and outside should be uniform between $-\pi$ and π as in Section 2.

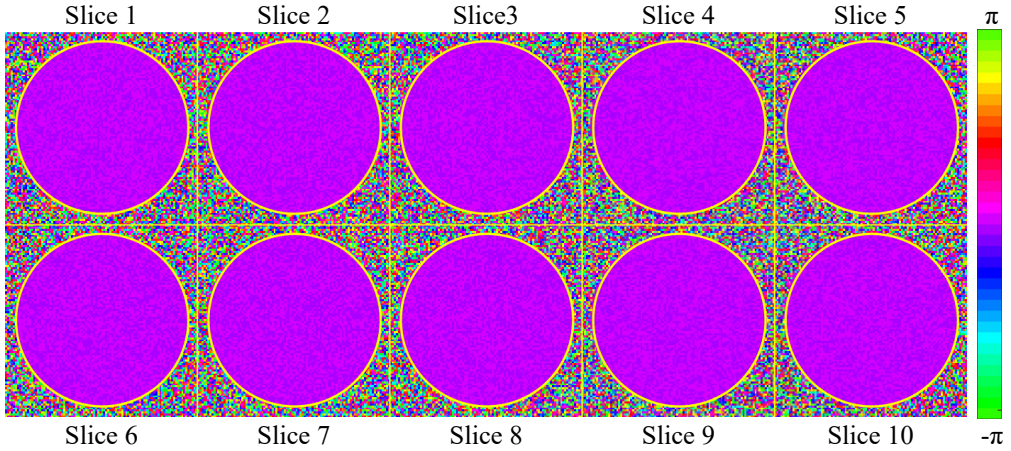

Figure 12: Phase slices of spherical agar phantom with RF off plus noise.

For the n_z=10 slices of the n_t=138 volume images, voxels were partitioned to be either inside the phantom or outside. Histograms of the voxels magnitudes both the within the phantom in red and outside the phantom in blue from all slices are in Figure 13 (left) along with the superimpose of the theoretical Ricean distribution inside and Rayleigh distribution outside as in Section 2. Note that the superimposed theoretical Rayleigh and Rice distributions fit the empirical histograms very well. This indicates that the real and imaginary parts of the images contain independent and identically distributed normal noise.

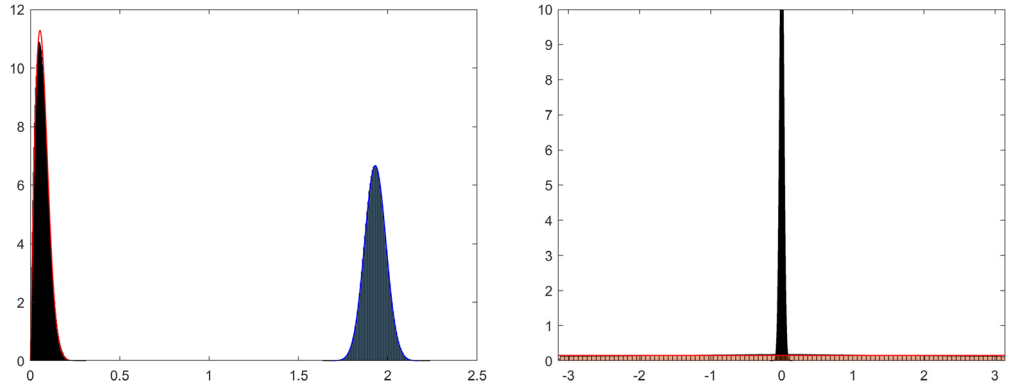

Figure 13: RF off plus signal histograms of magnitude (left) and phase (right) of spherical agar phantom.

Histograms of the voxels phases both the within and outside the phantom from all slices are in Figure 13 (right) along with the superimpose of the theoretical non-normal peaked distribution inside and uniform distribution outside. Note that the blue histogram with the superimposed theoretical non-normal peaked distribution inside and red histogram for the uniform between $-\pi$ and π outside distributions fit the theoretical distributions very well. This indicates that the real and imaginary parts of the images contain independent and identically distributed normal noise.

3.2 Real-Imaginary and AR(1) Correlations

In each voxel, there is a complex-valued time series formed from the series of complex-valued volume images. In each voxel of the n_z=10 slices, the correlation between the real and imaginary time series of length was computed and displayed in Figure 14. Note that in every voxel whether inside or outside the phantom the real-imaginary correlation is near zero. This indicates that the real and imaginary parts of the images contain independent and identically distributed normal noise.

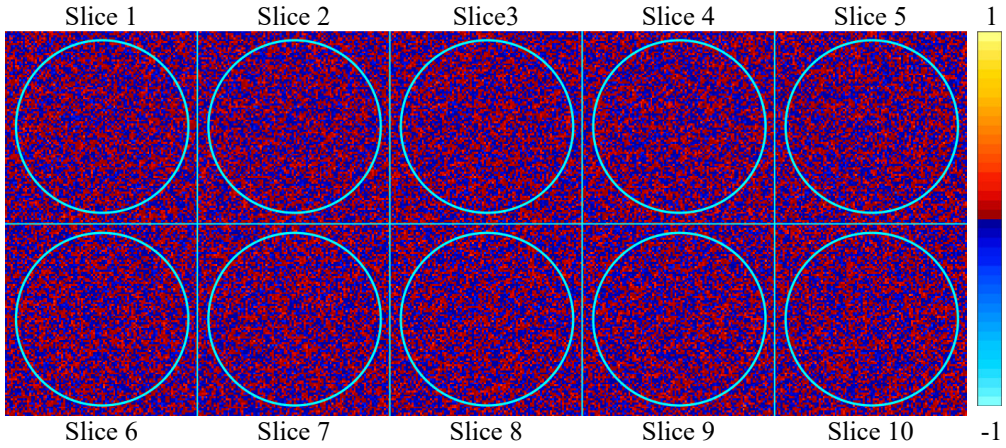

Figure 14: Real-imaginary correlation of spherical agar phantom with RF off plus signal.

In each voxel, the magnitude of the complex-valued time series was taken and the AR(1) autocorrelation computed as in Figure 15. Note that in every voxel whether inside or outside the phantom the magnitude AR(1) autocorrelation is near zero. This indicates that the real and imaginary parts of the images contain independent and identically distributed normal noise.

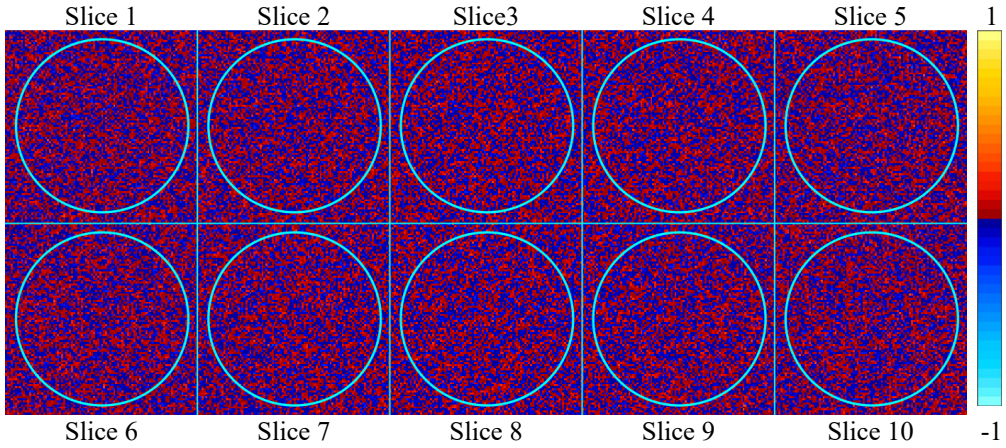

Figure 15: AR(1) magnitude correlation of spherical agar phantom with RF off plus signal.

To further examine these correlations, histograms were made. In Figure 16 (left) we can see that the real-imaginary correlations are centered about zero and appear to match the null hypothesis theoretical distribution superimposed in red. In Figure 16 (right) we can see that the AR(1) correlations in each voxel are centered about zero and appear to match the null hypothesis theoretical distribution superimposed in red. This indicates that the real and imaginary parts of the images are contain independent and identically distributed normal noise.

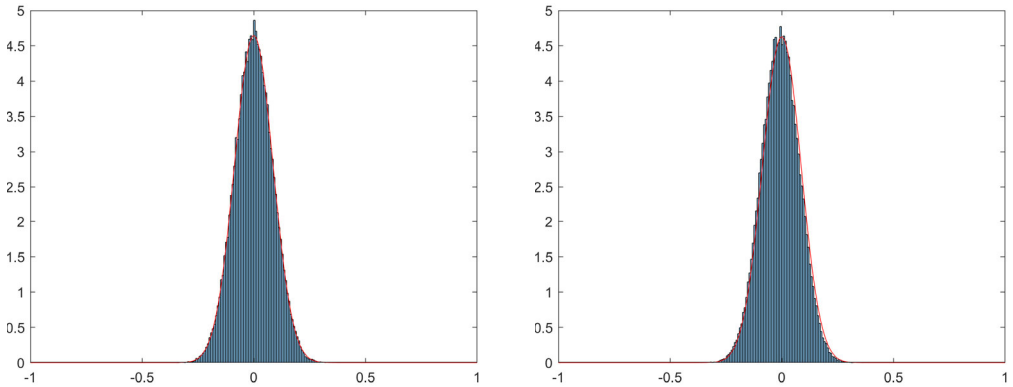

Figure 16: RF off plus signal histograms of real-imaginary (left) and AR(1) (right) correlations of the of spherical agar phantom.

From the graphical results presented in Figures 11-16, there is significant evidence to support the theoretical results that the complex-valued noise in voxels are independent and identically distributed from a normal distribution.

4. FMRI RF On Signal Data with Noise

After inverse Fourier transform reconstruction of the RF on *k*-space data, the images are again complex valued. The distribution of the magnitude and phase of the RF on fMRI data set will be examined in this section. The distribution of the voxel's magnitude, phase, correlation between their real and imaginary channels, and autocorrelation will be discussed.

4.1 Magnitude and Phase

The magnitude of the complex-valued slice images for the first time point, t=1, is presented in Figure 17. The magnitude images for all subsequent time points appear visually similar. Note that the magnitude values in the voxels inside the phantom are around 1.93 and outside are near zero.

This illustrates the fact that signal plus noise is being measured inside while pure noise is being measured outside. If the real and imaginary parts of the images are independent and identically distributed normal noise with constant mean, then the distribution of the magnitude should be Ricean distributed inside and outside should be Rayleigh as in Section 3.

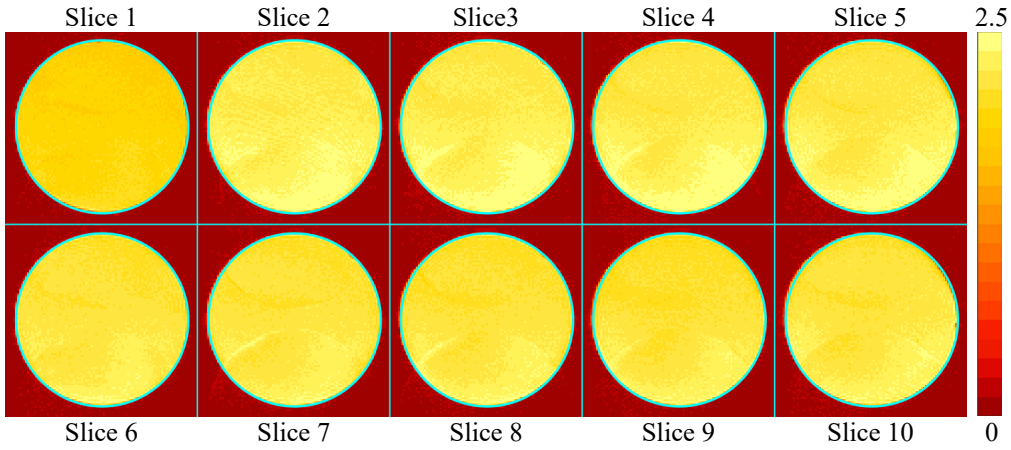

Figure 17: Magnitude slices of spherical agar phantom with RF on.

The phase of the complex-valued images for the first time point, t=1, is presented in Figure 18. The phase images for all subsequent time points appear visually similar. Note that the phase values in the voxels inside the phantom do not have a mean near zero and outside appear to have regions with Nyquist ghosting but also some voxels with random intensities between $-\pi$ and π as in Section 3. Inside the phantom, the magnetic field shim that is intended to produce a homogeneous magnetic field is imperfect. This is always a challenge experimentally, but usually relatively stable over time. This illustrates the fact that the phase inside the phantom is constant within a given voxel, varying spatially, and that pure noise is being measured outside if the Nyquist ghost can be properly corrected. If the real and imaginary parts of the images are independent and identically distributed normal noise with a constant magnitude for each voxel inside the phantom, then the distribution of the phase inside is not uniform but peaked about its mean (Rowe and Logan, 2004) and outside should be uniform between $-\pi$ and π as in Section 3 if it were not affected by ghosting.

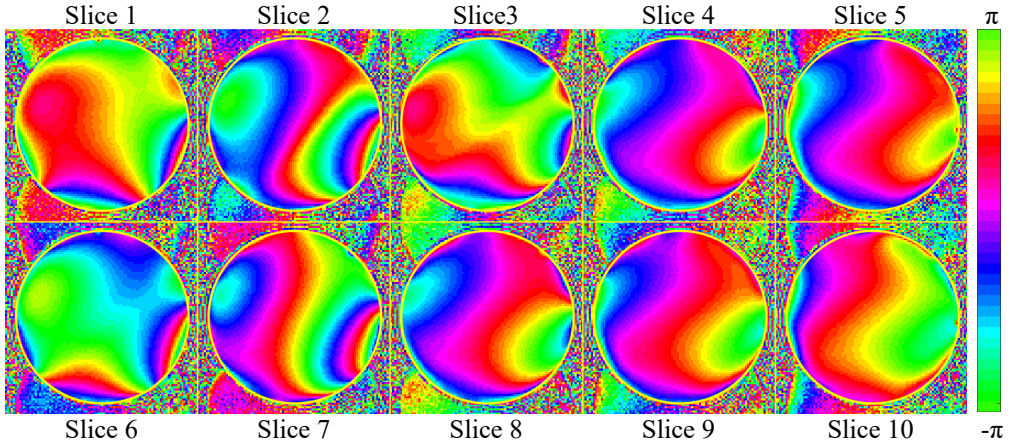

Figure 18: Phase slices of spherical agar phantom with RF on.

The angular mean phase of the n_t=138 complex-valued images was subtracted from each of the time point images. The demeaned volume phase image for the t=1 time point is presented in Figure 19. The phase images for all subsequent time points appear visually similar except varying outside the phantom. Note that the phase values in the voxels inside the phantom after being demeaned have a mean near zero and outside appear patterned from the Nyquist ghosting and not uniformly

distributed between $-\pi$ and π as in Section 3. This illustrates the fact that the RF on with subtracted mean phase inside the phantom and that pure noise is being measured outside except for Nyquist ghosting. If the real and imaginary parts of the images are independent and identically distributed normal noise with a constant magnitude inside, then the distribution of the phase inside is not uniform but peaked about its mean of zero here (Rowe and Logan, 2004) and outside should be uniform between $-\pi$ and π as in Section 3.

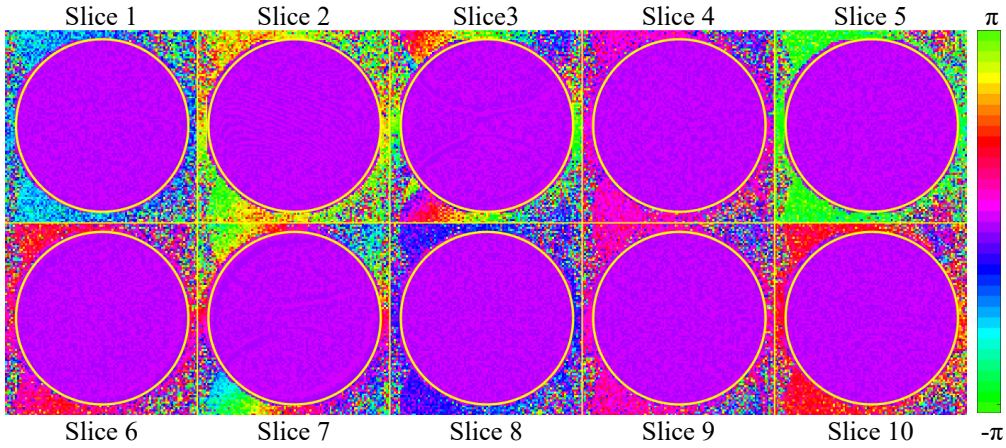

Figure 19: Phase slices of spherical agar phantom with RF off with voxel phase means subtracted.

For the n_z=10 slices of the n_t=138 volume images, voxels were partitioned to be either inside the phantom or outside. Histograms of the voxels magnitudes both the within the phantom in blue and outside the phantom in red from all slices are in Figure 20 (left). Note that the red histogram for the outside the phantom voxels in Figure 20 (left) appears to be Rayleigh like and the blue histogram for the inside the phantom appears to be Rice like as in Section 3. This indicates that the real and imaginary parts of the images are roughly independent and identically distributed normal noise.

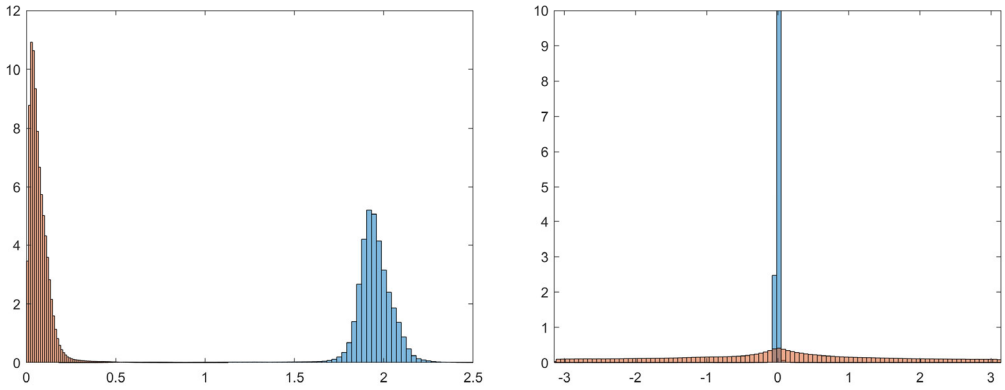

Figure 20: RF on histograms of magnitude (left) and phase (right) of spherical agar phantom.

Histograms of the voxels phases both the within and outside the phantom from all slices are in Figure 20 (right). Note that the histogram of inside voxel phases appear as a peaked distribution and uniform like between $-\pi$ and π. This indicates that the real and imaginary parts of the images are similar to independent and identically distributed normal noise.

4.2 Real-Imaginary and AR(1) Correlations

In each voxel, there is a complex-valued time series formed from the series of complex-valued volume images. In each voxel of the n_z=10 slices, the correlation between the real and imaginary time series of length was computed and displayed in Figure 21. Note that in most voxels whether inside or outside the phantom the real-imaginary correlation is near zero. However, because of the imperfect Nyquist ghost correction, there ire rings of high correlation predominantly in slices 3 and 7. The large number of near zero correlations indicates that the real and imaginary parts of the images contain predominantly independent and identically distributed normal noise, except for Nyquist ghost locations.

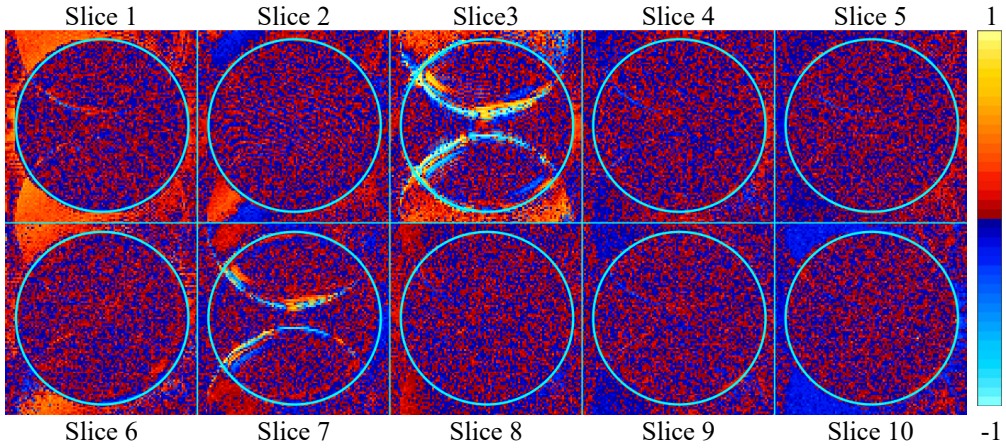

Figure 21: Real-imaginary correlation of spherical agar phantom with RF on.

In each voxel, the magnitude of the complex-valued time series was taken and the AR(1) autocorrelation computed as in Figure 22. Note that in most voxels whether inside or outside the phantom the magnitude AR(1) autocorrelation is near zero, except for Nyquist ghost locations. This provides evidence for believing that the real and imaginary parts of the images contain predominantly independent and identically distributed normal noise.

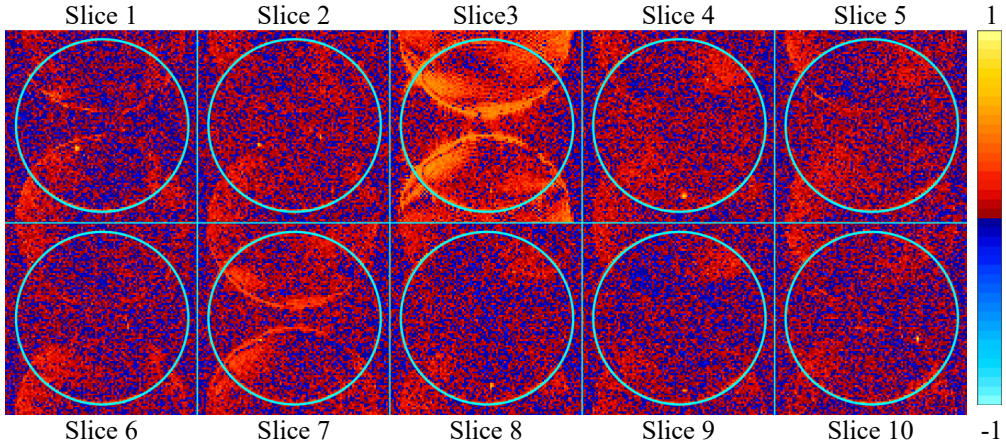

Figure 22: AR(1) magnitude correlation of spherical agar phantom with RF on.

To further examine these correlations, histograms were made. In Figure 23 (left) we can see that the real-imaginary correlations are mostly centered about zero and appear to match the null hypothesis theoretical distribution, however has heavier tails, especially in the positive direction due to the Nyquist ghosting primarily in slices 3 and 7 of Figure 21. In Figure 23 (right) we can see that the AR(1) correlations in the voxels are centered about zero and appear to match the null hypothesis theoretical distribution pretty well, except for an increased number of large positives primarily from

the Nyquist ghosting seen in slices 3 and 7 of Figure 22. This provides evidence that the real and imaginary parts of the images are contain independent and identically distributed normal noise.

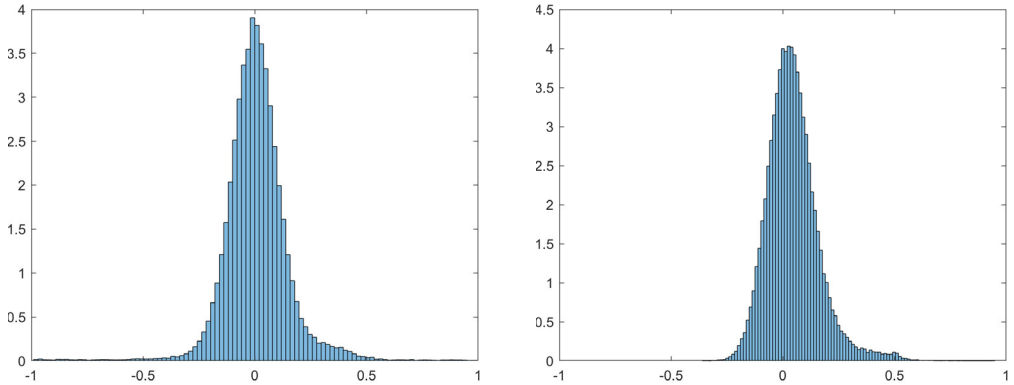

Figure 23: RF on histograms of real-imaginary (left) and AR(1) (right) correlations of the of spherical agar phantom.

From the graphical results presented in Figures 17-23, there is significant evidence to support the theoretical results that the complex-valued noise in voxels are independent and identically distributed from a normal distribution.

5. Discussion

Two fMRI data sets were acquired to examine the assumption of normally distributed noise in the real and imaginary channels of fMRI. It was found that then the RF is off and when artificial signal is added to the RF off data, the noise properties of the data follow the proper statistical distributions. However, when the RF is on, the Nyquist Ghost correction did not perform properly and resulted in residual signal. But there were good indications that the data would follow the proper distributions of the Nyquist ghost were properly corrected. This phantom is like a step function and difficult to remove ghosting. Always be sure to look at your images for potential artifacts. There many of possible sources of errors that are not seen and simply modeled. This data was from an old scanner that has been decommissioned. This data is very useful in illustrating the ideal data properties. Had the Nyquist ghost correction been able to work as designed, it can bee seen that the real and imaginary data well approximate observations from the normal distribution.

Acknowledgements

I would like to thank Professor Andrew Nencka at the Medical College of Wisconsin for the data.

References

1. Rowe DB. Image Reconstruction in Functional MRI (2016). In Handbook of Statistical Methods for Brain Signals and Images, Chapman & Hall/CRC Press, p205-232. ISBN: 978-1-4822-20971
2. Huttel SA, Song A, McCarthy G. *Functional Magnetic Resonance Imaging* (2004). Sinauer Publishers, 2004. ISBN 0-87893-288-7
3. Rowe DB, Logan BR. *A complex way to compute fMRI activation* (2004). Neuroimage. 2004 Nov;23(3):1078-92.